



An elasto-viscoplastic interface model for investigating the constitutive behavior of nacre

H. Tang, F. Barthelat, H.D. Espinosa*

Northwestern University, Mechanical Engineering, 2145 Sheridan Road, Evanston IL 60208-3111, USA

Received 12 September 2006; received in revised form 9 November 2006; accepted 27 December 2006

Abstract

In order to better understand the strengthening mechanism observed in nacre, we have developed an interface computational model to simulate the behavior of the organic present at the interface between aragonite tablets. In the model, the single polymer-chain behavior is characterized by the worm-like-chain (WLC) model, which is in turn incorporated into the eight-chain cell model developed by Arruda and Boyce [Arruda, E.M., Boyce, M.C., 1993a. A three-dimensional constitutive model for the large stretches, with application to polymeric glasses. *Int. J. Solids Struct.* 40, 389–412] to achieve a continuum interface constitutive description. The interface model is formulated within a finite-deformation framework. A fully implicit time-integration algorithm is used for solving the discretized governing equations.

Finite element simulations were performed on a representative volume element (RVE) to investigate the tensile response of nacre. The staggered arrangement of tablets and interface waviness obtained experimentally by Barthelat et al. [Barthelat, F., Tang, H., Zavattieri, P.D., Li, C.-M., Espinosa, H.D., 2007. On the mechanics of mother-of-pearl: a key feature in the material hierarchical structure. *J. Mech. Phys. Solids* 55 (2), 306–337] was included in the RVE simulations. The simulations showed that both the rate-dependence of the tensile response and hysteresis loops during loading, unloading and reloading cycles were captured by the model. Through a parametric study, the effect of the polymer constitutive response during tablet-climbing and its relation to interface hardening was investigated. It is shown that stiffening of the organic material is not required to achieve the experimentally observed strain hardening of nacre during tension. In fact, when ratios of contour length/persistent length experimentally identified are employed in the simulations, the predicted stress–strain behavior exhibits a deformation hardening consistent with the one measured experimentally and also captured by the phenomenological cohesive model used in the study carried out by Barthelat et al. [Barthelat, F., Tang, H., Zavattieri, P.D., Li, C.-M., Espinosa, H.D., 2007. On

*Corresponding author.

E-mail address: espinosa@northwestern.edu (H.D. Espinosa).

the mechanics of mother-of-pearl: a key feature in the material hierarchical structure. *J. Mech. Phys. Solids* 55 (2), 306–337]. The simulation results also reveal that the bulk modulus of the polymer controls the rate of hardening, feature not captured by more simple cohesive laws.

© 2007 Elsevier Ltd. All rights reserved.

Keywords: Elasto-viscoplasticity; Interface model; Nacre; Biological materials; Biomechanics

1. Introduction

Nacre is composed of a “brick-and-mortar” microstructure of ~95 vol% mineral (aragonite, the bricks) and ~5 vol% protein-rich organic material (the mortar). The mineral is very brittle and unsuitable as a structural material. Amazingly, nacre can still sustain significant inelastic deformation and exhibit toughness 20–30 times that of aragonite. The superior properties of nacre are mainly attributed to its hierarchical microstructure, which has developed through millions of years of evolution and natural selection. Within this hierarchy, large aspect-ratio mineral tablets are closely stacked in a staggered alignment and organic material acts as an adhesive gluing the tablets together. Understanding the structure–property relationship of nacre based on these features has been the subject of considerable research within the mechanics community because of its relevance in the design of new synthetic materials. A great number of experiments and simulations (Currey, 1977; Jackson et al., 1988; Menig et al., 2000; Wang et al., 2001; Barthelat et al., 2006, 2007) have been conducted using a variety of experimental techniques and numerical models to elucidate the deformation mechanisms present in nacre. From these studies it is believed that the interface behavior holds the key to the material outstanding properties (Wang et al., 2001; Ji and Gao, 2004; Barthelat et al., 2006, 2007). In this regard, the organic material appears to be responsible for the strong strain rate sensitivity and viscoplasticity exhibited by nacre (Currey, 1977; Menig et al., 2000). Nanoscale asperities on the tablet surfaces were shown to provide resistance to inter-lamellar sliding and to strengthen the material (Evans et al., 2001; Wang et al., 2001). Clearly, detailed modeling of the interface behavior of nacre is crucial, but it presents particular challenges. There are difficulties associated with the description of the constitutive behavior of the organic material, which is subjected to strong confinement resulting from the small interlayer thickness between relatively rigid mineral tablets. Handling of surface topology at the interface also presents some challenges.

Katti et al. (2001) simulated the material response of nacre using a three-dimensional (3D) finite element model. In their model, the organic interlayer was simulated using continuum elements within the context of the conventional J2 plasticity theory. The model was phenomenological, and the polymer deformation behavior of the organic material was not accounted for.

The deformation behavior of the organic material (proteins) was investigated in a series of axial force–extension experiments conducted by Smith et al. (1999). Irregular “saw-tooth” type force–displacement curves were identified in the experiments. The response was attributed to the sequential force-induced unfolding of the Lustrin A protein. Qi et al. (2005) proposed a hyperelastic model intended to capture the special mechanical behavior exhibited by the Lustrin A protein. Their numerical simulations of tensile extension of representative

volume elements (RVEs) of nacre showed that the progressive unfolding of molecules in the organic matrix contributed to macroscopic softening, ensuring larger deformations without catastrophic failure. In [Ji and Gao \(2004\)](#), the organic matrix was simulated using the virtual internal bond (VIB) model to investigate fracture behavior. The effects of surface topology at interface were ruled out in these models. In [Barthelat et al. \(2006, 2007\)](#), the surface waviness of tablets were explicitly simulated to capture the effects of surface topology on the mechanical behavior of nacre. In their model, a rate-independent interface constitutive law ([Camacho and Ortiz, 1996](#); [Espinosa and Zavattieri, 2003](#)) was used to characterize the mechanical behavior of the organic material. It was shown that the microscopic waviness of the tablets was a key to progressive tablet locking and local hardening, a fundamental requirement for the spreading of deformations over large volumes.

In order to better understand the experimental findings and clarify the roles of structure and material constituents in the mechanical behavior of nacre, there is a need to develop accurate and robust numerical models for this material. For instance, hardening of the biopolymer at large strains and its viscoplastic response need to be accurately modeled. In addition, the effects of stress triaxiality on the interface behavior are generally ruled out in the conventional cohesive zone methods ([Tvergaard and Hutchinson, 1992](#); [Xu and Needleman, 1994](#)). We believe that this effect may be important and should be accounted for to better understand the mechanical behavior of nacre and the underlying mechanisms.

In the present study, we propose an interface model motivated by the relevant micromechanisms controlling the deformation behavior of the organic material in nacre. The interface model is intended to simulate the polymer deformation behavior for a finite interface thickness. The organic interlayer of nacre is assumed to behave like amorphous biopolymers, gluing mineral tablets together. In this regard, we treat the elasto-viscoplastic behavior of the organic material in a unified manner through constitutive modeling. The constitutive description used here is similar to the one widely used for glassy polymers ([Parks et al., 1984](#); [Arruda and Boyce, 1993b](#); [Wu and van der Giessen, 1993](#)). Unlike polymer chains in rubber-like materials, which have an uncorrelated nature represented by the freely-jointed-chain (FJC) model ([Arruda and Boyce, 1993a](#)), biological chains are generally considered correlated with a smoother chain configuration. We use the worm-like-chain (WLC) model ([Oberhauser et al., 1998](#); [Bao and Suresh, 2003](#); [Kuhl et al., 2005](#)) to simulate the single-chain behavior of polymeric fibrils in the organic material of nacre. The single-chain behavior is incorporated into the Arruda–Boyce eight-chain model ([Arruda and Boyce, 1993a](#)) to obtain a continuum constitutive description.

This paper is organized as follows. In Section 2, we discuss the principle of virtual work for an RVE of nacre within the framework of finite deformation. In Section 3, we describe the constitutive formulations for the organic material. The numerical implementation of the interface model is elaborated in Section 4. In Section 5, we conduct a parametric study for the WLC model to show the effect of model parameters on the material response. In Section 6, we demonstrate the predictive capabilities of the interface model in simulating the mechanical behavior of nacre. Their relevance to strengthening mechanisms is highlighted. In Section 7, we conclude with final remarks and future studies on the interface model.

2. Interface model within the framework of finite deformation

The “brick-and-mortar” structure of nacre is illustrated in [Fig. 1](#). In this structure, the organic interlayer (approximately 20–50 nm thickness) serves as a polymer adhesive

between individual tablets (0.2–0.5 μm thick). For such two-phase composite material in equilibrium, the principle of virtual work is written in the form

$$\int_{B_0^I} \mathbf{P} : \delta \dot{\mathbf{F}} dV + \int_{B_0^O} \mathbf{P} : \delta \dot{\mathbf{F}} dV - \int_{\partial B_0^I} \mathbf{T} \cdot \delta \mathbf{v} dS - \int_{B_0} \mathbf{B} \cdot \delta \mathbf{v} dV = 0, \tag{1}$$

where \mathbf{P} is the first Piola–Kirchhoff stress, $\delta \dot{\mathbf{F}}$ the virtual rate of deformation gradient, \mathbf{T} and \mathbf{B} are the externally applied tractions and body forces defined on the reference configuration, respectively, and $\delta \mathbf{v}$ is the virtual velocity. Furthermore, the integration domain is B_0 with ∂B_0^I the external surface area over which the external tractions are applied, both defined in the reference configuration. In Eq. (1), B_0 consists of two parts, B_0^I and B_0^O , representing the total volume of the inorganic tablets and the organic matrix, respectively.

In formulating the interface model, we start from the internal virtual work associated to the organic matrix, viz.,

$$\delta W^{\text{Inter}} = \int_{B_0^O} \mathbf{P} : \delta \dot{\mathbf{F}} dV. \tag{2}$$

In Fig. 2, a 2D microstructure of nacre as represented by a two-phase composite is illustrated. The interlayer thickness, H , is assumed to be uniform as shown in the plot. Generalization to a variable thickness is trivial within the framework of finite elements as will be illustrated later. Since the thickness of the interlayer is much smaller than that of the mineral tablets, the deformation through the thickness of the interlayer is assumed to be uniform. In addition, the in-plane transverse deformation of the interface material is constrained due to the confinement of the interlayer material between relatively rigid

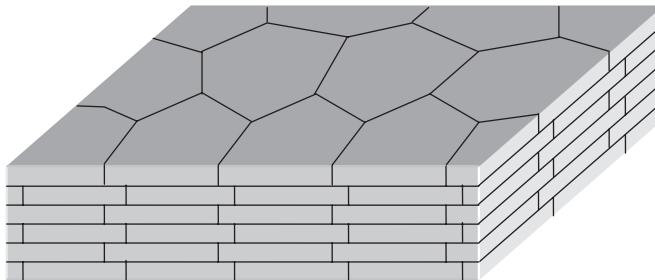


Fig. 1. Sketch of nacre “brick and mortar” microstructure. The mineral tablets are embedded in an organic matrix.

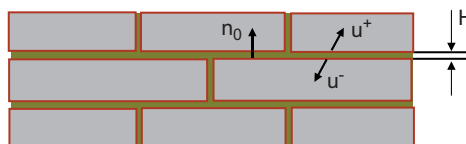


Fig. 2. A 2D illustration of the microstructure of nacre. u^+ and u^- refer to the displacements on the top and bottom surfaces of the interlayer, respectively. The normal to the interface is \mathbf{n}_0 , defined on the reference configuration. The thickness of the interlayer is denoted by H .

tablets. The deformation gradient of the interlayer is therefore taken to have the form

$$\mathbf{F} = \mathbf{I} + \frac{\Delta \otimes \mathbf{n}_0}{H}, \quad (3)$$

where \mathbf{I} is the identity tensor, \mathbf{n}_0 the outer normal of bottom surface S^- pointing to the top surface S^+ defined on the reference configuration, and $\Delta = \mathbf{u}^+ - \mathbf{u}^-$ is the displacement difference across the interlayer (see Fig. 2). Combining Eqs. (2) and (3), the internal virtual work of the organic matrix is expressed as

$$\delta W^{\text{Inter}} = \int_{B_0^O} \mathbf{P} : \frac{\delta \dot{\Delta} \otimes \mathbf{n}_0}{H} dV = \int_{\Gamma_0} \mathbf{T} \delta \dot{\Delta} d\Gamma_0, \quad (4)$$

where $\mathbf{T} = \mathbf{P} \cdot \mathbf{n}_0$ is the traction on the bottom surface S^- with the undeformed area Γ_0 . The interface model as represented by Eq. (4) is implemented as a user-defined interface element within the commercial FEM code ABAQUS (2004). In contrast to conventional interface models, which generally use phenomenological traction-separation relations, we consider the elasto-viscoplastic behavior of the organic material in a unified manner through constitutive modeling. More details on the constitutive modeling are discussed in the subsequent section.

The thickness of the interface element in the numerical implementation is taken to be zero. Instead, the interlayer thickness, H , is treated as an intrinsic material parameter which is included in the constitutive laws. To prevent interpenetration between top and bottom surfaces of the interface element, we use the penalty method with the constraint condition, $\hat{\Delta}_n \geq -\Delta_{\text{cr}}$, where $\hat{\Delta}_n$ is the normal separation of the interface element and Δ_{cr} is a critical displacement jump controlling the deformation level at which interface compression is allowed. In this manner, the effect of interface compliance on the mechanical behavior of nacre is accounted for. Suitable choices for Δ_{cr} will be discussed later. According to this approach, the internal virtual work of the organic matrix for $\hat{\Delta}_n \leq -\Delta_{\text{cr}}$, is expressed as

$$\delta W^{\text{Inter}} = \int_{\partial B_0^O} \mathbf{T} \cdot \delta \dot{\Delta} d\Gamma_0 + \int_{\partial B_0^O} K (\hat{\Delta}_n + \Delta_{\text{cr}}) \cdot \delta \hat{\Delta}_n d\Gamma_0, \quad (5)$$

where K is the penalty number.

The climbing of tablets during tension or shear parallel to tablet planes is a salient feature of the deformation behavior of nacre associated with its morphological structure. Hence, it is crucial to accurately model this deformation behavior in order to elucidate the strengthening mechanisms present in nacre. In this regard, the penalty method ensures that tablet climbing associated with the relative sliding between overlapped wavy tablets is effectively modeled.

3. Interface constitutive formulations

Nacre exhibits significant strain rate sensitivity and viscoplasticity. This is mainly attributed to the polymer deformation behavior of the organic matrix. Here, we use an elasto-viscoplastic constitutive model to characterize the mechanical behavior of the organic material. In the constitutive descriptions, the WLC model is incorporated through the definition of a back stress to reflect the effects of polymer stiffening with increased

deformation. This has been motivated by the work of Parks et al. (1984) and Arruda and Boyce (1993b). In their studies, the FJC model was considered.

3.1. Kinematics

The deformation gradient, \mathbf{F} , is multiplicatively decomposed into an elastic part \mathbf{F}^e and a plastic part \mathbf{F}^p with the form

$$\mathbf{F} = \mathbf{F}^e \mathbf{F}^p. \tag{6}$$

The elastic part of the deformation gradient is written as

$$\mathbf{F}^e = \mathbf{R}^e \mathbf{U}^e = \mathbf{V}^e \mathbf{R}^e, \tag{7}$$

where \mathbf{R}^e is the elastic rotation tensor, \mathbf{U}^e the right elastic stretch tensor, and \mathbf{V}^e the left elastic stretch tensor. The logarithmic elastic strain is defined as $\overline{\mathbf{E}}_{(0)}^e = \ln \mathbf{U}^e$. Similarly, for the plastic part of the deformation gradient, we have

$$\mathbf{F}^p = \mathbf{R}^p \mathbf{U}^p = \mathbf{V}^p \mathbf{R}^p, \tag{8}$$

where \mathbf{R}^p is the plastic rotation tensor, \mathbf{U}^p the right plastic stretch tensor, and \mathbf{V}^p the left plastic stretch tensor. Furthermore, $\mathbf{b}^p = \mathbf{F}^p \mathbf{F}^{pT} = (\mathbf{V}^p)^2$ is the plastic left Cauchy–Green deformation tensor. The plastic velocity gradient, $\overline{\mathbf{L}}^p$, which is defined on the intermediate configuration, takes the form

$$\overline{\mathbf{L}}^p = \overline{\mathbf{D}}^p + \overline{\mathbf{W}}^p = \dot{\mathbf{F}}^p \mathbf{F}^{p-1}, \tag{9}$$

where $\overline{\mathbf{D}}^p$ and $\overline{\mathbf{W}}^p$ are the plastic rate of deformation and the plastic spin defined on the intermediate configuration, respectively. The velocity gradient, \mathbf{l} , defined in the current configuration is

$$\mathbf{l} = \dot{\mathbf{F}} \mathbf{F}^{-1} = \mathbf{d} + \mathbf{w} = \dot{\mathbf{F}}^e \mathbf{F}^{e-1} + \mathbf{F}^e \overline{\mathbf{L}}^p \mathbf{F}^{e-1}, \tag{10}$$

where $\mathbf{d} = 1/2(\mathbf{l} + \mathbf{l}^T)$ is the rate of deformation and $\mathbf{w} = 1/2(\mathbf{l} - \mathbf{l}^T)$ is the spin. With the assumption $\overline{\mathbf{W}}^p = 0$ (Weber and Anand, 1990), the rate of deformation is further written as

$$\mathbf{d} = \mathbf{d}^e + \text{sym}(\mathbf{F}^e \overline{\mathbf{D}}^p \mathbf{F}^{e-1}), \tag{11}$$

where

$$\mathbf{d}^e = 1/2(\dot{\mathbf{F}}^e \mathbf{F}^{e-1} + \mathbf{F}^{e-T} \dot{\mathbf{F}}^{eT}). \tag{12}$$

3.2. Constitutive descriptions within a finite-deformation framework

It is postulated that there exists a Helmholtz free-energy function defined per unite reference volume which takes the non-interactive form (Anand and Gurtin, 2003)

$$\Psi(\overline{\mathbf{E}}_{(0)}^e, \mathbf{b}^p) = \Psi^e(\overline{\mathbf{E}}_{(0)}^e) + \Psi^p(\mathbf{b}^p), \tag{13}$$

where Ψ^e is an elastic free energy and Ψ^p is a plastic free energy. For the isothermal process, the Clausius–Duhem dissipation inequality is taken to have the form (Holzapfel, 2000)

$$\boldsymbol{\tau} : \mathbf{d} - \dot{\Psi}(\overline{\mathbf{E}}_{(0)}^e, \mathbf{b}^p) \geq 0, \tag{14}$$

where τ is the Kirchhoff stress and

$$\dot{\Psi}(\bar{\mathbf{E}}_{(0)}^e, \mathbf{b}^p) = \frac{\partial \Psi^e}{\partial \bar{\mathbf{E}}_{(0)}^e} : \dot{\bar{\mathbf{E}}}_{(0)}^e + 2 \frac{\partial \Psi^p}{\partial \mathbf{b}^p} \mathbf{b}^p : \bar{\mathbf{D}}^p. \tag{15}$$

Combining Eqs. (11), (14) and (15), it is shown that the dissipation inequality has the form

$$\left\{ \mathbf{R}^{eT} \tau \mathbf{R}^e : \mathbf{R}^{eT} \mathbf{d}^e \mathbf{R}^e - \frac{\partial \Psi^e}{\partial \bar{\mathbf{E}}_{(0)}^e} : \dot{\bar{\mathbf{E}}}_{(0)}^e \right\} + \left(\mathbf{F}^{eT} \tau \mathbf{F}^{e-T} - 2 \frac{\partial \Psi^p}{\partial \mathbf{b}^p} \mathbf{b}^p \right) : \bar{\mathbf{D}}^p \geq 0. \tag{16}$$

With the assumption that the elastic stretch is small in the sense that $\mathbf{U}^e \doteq \mathbf{I}$, where \mathbf{I} is the second-order identity tensor, we have (Lubarda, 2002)

$$\dot{\bar{\mathbf{E}}}_{(0)}^e \doteq \mathbf{R}^{eT} \mathbf{d}^e \mathbf{R}^e \tag{17}$$

and

$$\bar{\tau} = \mathbf{R}^{eT} \tau \mathbf{R}^e \doteq \mathbf{F}^{eT} \tau \mathbf{F}^{e-T}. \tag{18}$$

We define back stress as (Anand and Gurtin, 2003)

$$\bar{\mathbf{B}} = 2 \frac{\partial \Psi^p}{\partial \mathbf{b}^p} \mathbf{b}^p. \tag{19}$$

Noting that $\bar{\mathbf{D}}^p$ is a deviatoric tensor, we therefore rewrite Eq. (16) as

$$\left(\bar{\tau} - \frac{\partial \Psi^e}{\partial \bar{\mathbf{E}}_{(0)}^e} \right) : \dot{\bar{\mathbf{E}}}_{(0)}^e + (\bar{\tau}' - \bar{\mathbf{B}}') : \bar{\mathbf{D}}^p \geq 0, \tag{20}$$

where $\bar{\tau}' = \bar{\tau} - (1/3)\text{tr}(\bar{\tau})\mathbf{I}$, and $\bar{\mathbf{B}}' = \bar{\mathbf{B}} - (1/3)\text{tr}(\bar{\mathbf{B}})\mathbf{I}$ are the deviatoric parts of $\bar{\tau}$ and the back stress, $\bar{\mathbf{B}}$, respectively. To ensure the inequality, we have

$$\bar{\tau} = \frac{\partial \Psi^e}{\partial \bar{\mathbf{E}}_{(0)}^e} \tag{21}$$

and the evolution relation for plastic strain is defined as

$$\bar{\mathbf{D}}^p = \dot{\gamma} \bar{\mathbf{N}}, \tag{22}$$

where $\dot{\gamma}$ is the plastic shear rate, and

$$\bar{\mathbf{N}} = \frac{\bar{\tau}' - \bar{\mathbf{B}}'}{\sqrt{2\bar{\tau}}} \tag{23}$$

with $\bar{\tau}_{\text{eff}} = \sqrt{\frac{1}{2}(\bar{\tau}' - \bar{\mathbf{B}}') : (\bar{\tau}' - \bar{\mathbf{B}}')}$, is the tensorial direction of plastic flow. In the present study, the plastic shear rate is assumed to take the power-law form

$$\dot{\gamma} = \dot{\gamma}_0 \left(\frac{\bar{\tau}_{\text{eff}}}{s} \right)^{1/m}, \tag{24}$$

where m is the material rate sensitivity constant, with $m = 0$ denoting the rate-independent limit, s is the flow resistance to the deformation of the organic material which is taken to be constant in the study conducted here, and $\dot{\gamma}_0$ is the reference shear rate.

We define the elastic free energy as

$$\Psi^e(\bar{\mathbf{E}}_{(0)}^e) = \frac{1}{2} \bar{\mathbf{E}}_{(0)}^e : \underline{\underline{\mathbf{L}}} : \bar{\mathbf{E}}_{(0)}^e, \quad (25)$$

where $\underline{\underline{\mathbf{L}}}$ is the fourth-order isotropic elastic modulus which has the form

$$\underline{\underline{\mathbf{L}}} = 2\mu \mathbf{II} + (k - 2/3\mu) \mathbf{I} \otimes \mathbf{I}, \quad (26)$$

where \mathbf{II} is the fourth-order symmetric identity tensor, μ the elastic shear modulus, and k the elastic bulk modulus. As a result, the constitutive equation for stress takes the form

$$\bar{\boldsymbol{\tau}} = \underline{\underline{\mathbf{L}}} : \bar{\mathbf{E}}_{(0)}^e. \quad (27)$$

3.3. Macroscopic plastic free energy

In this study, the back stress is determined by the accumulated plastic stretch, \mathbf{V}^p , reflecting the orientation-dependent strain hardening of the organic material as the polymer chains tend to align along the directions of the largest plastic stretch (Arruda and Boyce, 1993b). Here, the mechanical behavior of a single biopolymer chain is incorporated into the overall constitutive description of the organic material according to the Arruda–Boyce eight-chain model (Arruda and Boyce, 1993a; Bischoff et al., 2002; Kuhl et al., 2005). This is essentially a non-affine model with the assumption that the eight-chain unit cell is instantaneously aligned with the directions of principal stretches once deformation is applied.

Proteins have been shown to be important load-carrying components of the organic material in nacre (Smith et al., 1999). In the study of biological materials, the WLC model is often used to characterize the mechanical behavior of a single protein molecule (Bao and Suresh, 2003). The parameters used in the WLC model include the contour length, L_c , and the persistence length p . The contour length, L_c , is the length of chains at full extension, and plays significant roles on the entropic elasticity behavior of single molecules. The persistence length is understood as the sum of the average projection of all bonds onto the direction of the first bond. The force–stretch relation for a single wormlike chain is usually taken to have the form (Marko and Siggia, 1995)

$$f^{\text{WLC}}(r) = \frac{k\theta}{4p} \left[4 \frac{r}{L_c} + \frac{1}{(1 - r/L_c)^2} - 1 \right], \quad (28)$$

where r is the end-to-end distance of a single chain. By integrating the force about r , it is easy to show that the free energy of a single WLC has the form

$$\psi(r) = \frac{k\theta L_c}{4p} \left[2 \frac{r^2}{L_c^2} - \frac{r}{L_c} + \frac{1}{1 - r/L_c} \right] + \psi_0, \quad (29)$$

where ψ_0 corresponds to the contribution from the initial entropy of the molecule. Based on the Arruda–Boyce 8-chain cell model, the I_1^p -based plastic free energy for the organic material is shown to take the form

$$\Psi^p(I_1^p) = \frac{\mu_R A}{4} \left[4 \frac{\lambda_{\text{chain}}^2}{A} - \lambda_{\text{chain}} \sqrt{\frac{2}{A}} + \frac{1}{1 - \lambda_{\text{chain}} \sqrt{2/A}} \right] + \Psi_0, \quad (30)$$

where $\Lambda = L_c/p$, $\lambda_{\text{chain}} = \sqrt{I_1^p/3}$ is the stretch of each chain in the 8-chain unit cell, $\mu_R = nk\theta$ with n the chain density, k the Boltzmann's constant, and θ the temperature, and $\Psi_0 = m/\rho_0$. Here, the undeformed length of each chain in the 8-chain cell is taken to be $r_0 = \sqrt{2L_c p}$ for the WLC model (Marko and Siggia, 1995; Bischoff et al., 2002). According to the definition, we must have $\Lambda \geq 2$, otherwise the undeformed chain length will be greater than the contour length. The locking stretch at full extension of chains can be defined as $\lambda_L = L_c/r_0$, which is equal to $\sqrt{\Lambda/2}$.

4. Time-integration procedure

4.1. Time-integration procedure of interface constitutive equations

It is assumed that a series of variables, $\bar{\boldsymbol{\tau}}(t)$, $\bar{\mathbf{B}}'(t)$ and $\mathbf{F}^p(t)$, are known at time t . For given $\mathbf{F}(\tau)$ at time $\tau = t + \Delta t$, we need to find $\bar{\boldsymbol{\tau}}(\tau)$, $\bar{\mathbf{B}}'(\tau)$ and $\mathbf{F}^p(\tau)$. Integrating Eq. (9), we have

$$\mathbf{F}^p(\tau) = \exp(\Delta t \bar{\mathbf{D}}^p(\tau)) \mathbf{F}^p(t), \quad (31)$$

where $\bar{\mathbf{D}}^p(\tau) = \dot{\gamma}(\bar{\boldsymbol{\tau}}(\tau), \bar{\mathbf{B}}'(\tau)) \bar{\mathbf{N}}(\tau)$. The elastic part of the deformation gradient, $\mathbf{F}^e(\tau)$, is obtained by

$$\mathbf{F}^e(\tau) = \mathbf{F}_{\text{tr}}^e \exp(-\Delta t \bar{\mathbf{D}}^p(\tau)), \quad (32)$$

where $\mathbf{F}_{\text{tr}}^e = \mathbf{F}(\tau) \mathbf{F}^p(\tau)^{-1}$ is a trial value of the elastic part of the deformation gradient. As shown in Weber and Anand (1990), the elastic strain at time τ is updated as

$$\bar{\mathbf{E}}_{(0)}^e(\tau) = \bar{\mathbf{E}}_{\text{tr}}^e - \Delta t \bar{\mathbf{D}}^p(\tau), \quad (33)$$

where $\bar{\mathbf{E}}_{\text{tr}}^e = \ln \mathbf{U}_{\text{tr}}^e$, with $\mathbf{U}_{\text{tr}}^{e2} = \mathbf{F}_{\text{tr}}^{eT} \mathbf{F}_{\text{tr}}^e$, is the trial elastic strain. Combining Eqs. (33) and (27), the stress update at time τ takes the form

$$\bar{\boldsymbol{\tau}}(\tau) = \bar{\boldsymbol{\tau}}_{\text{tr}} - \underline{\underline{\mathbf{L}}} : [\Delta t \bar{\mathbf{D}}^p(\tau)] = \bar{\boldsymbol{\tau}}_{\text{tr}} - \underline{\underline{\mathbf{L}}} : [\Delta t \dot{\gamma}(\bar{\boldsymbol{\tau}}(\tau), \bar{\mathbf{B}}'(\tau)) \bar{\mathbf{N}}(\tau)], \quad (34)$$

where

$$\bar{\boldsymbol{\tau}}_{\text{tr}} = \mathbf{L} : \bar{\mathbf{E}}_{\text{tr}}^e. \quad (35)$$

The deviatoric part of the back stress is updated as

$$\bar{\mathbf{B}}'(\tau) = \underline{\underline{\mathbf{P}}} : 2 \frac{\partial \Psi^p(I_1^p(\tau))}{\partial I_1^p} \mathbf{b}^p(\tau), \quad (36)$$

where $\underline{\underline{\mathbf{P}}} = \mathbf{II} - (1/3)\mathbf{I} \otimes \mathbf{I}$ is the fourth-order deviatoric tensor.

Eqs. (34) and (36) are expressed in their residual forms as

$$\mathbf{R}_1(\bar{\boldsymbol{\tau}}(\tau), \bar{\mathbf{B}}'(\tau)) = \bar{\boldsymbol{\tau}}(\tau) - \bar{\boldsymbol{\tau}}_{\text{tr}} + \mathbf{L} : [\Delta t \dot{\gamma}(\bar{\boldsymbol{\tau}}(\tau), \bar{\mathbf{B}}'(\tau)) \bar{\mathbf{N}}(\tau)] \quad (37)$$

and

$$\mathbf{R}_2(\bar{\boldsymbol{\tau}}(\tau), \bar{\mathbf{B}}'(\tau)) = \bar{\mathbf{B}}'(\tau) - \underline{\underline{\mathbf{P}}} : 2 \frac{\partial \Psi^p(I_1^p(\tau))}{\partial I_1^p} \mathbf{b}^p(\tau), \quad (38)$$

respectively. A generic Newton–Raphson method is used to solve the equations

$$\begin{cases} \mathbf{R}_1(\bar{\boldsymbol{\tau}}(\tau), \bar{\mathbf{B}}'(\tau)) = 0, \\ \mathbf{R}_2(\bar{\boldsymbol{\tau}}(\tau), \bar{\mathbf{B}}'(\tau)) = 0. \end{cases} \tag{39}$$

During the iteration α of a Newton–Raphson procedure, the following linear system is solved:

$$\begin{bmatrix} \bar{\boldsymbol{\tau}}(\tau) \\ \bar{\mathbf{B}}'(\tau) \end{bmatrix}^{\alpha+1} = \begin{bmatrix} \bar{\boldsymbol{\tau}}(\tau) \\ \bar{\mathbf{B}}'(\tau) \end{bmatrix}^{\alpha} - \mathbf{G}^{\alpha}(\tau)^{-1} : \begin{bmatrix} \mathbf{R}_1(\tau) \\ \mathbf{R}_2(\tau) \end{bmatrix}^{\alpha}, \tag{40}$$

where

$$\mathbf{G}^{\alpha}(\tau) = \begin{bmatrix} \mathbf{II} + \underline{\underline{\mathbf{L}}}: \left(\bar{\mathbf{N}} \otimes \frac{\partial \Delta\gamma}{\partial \bar{\boldsymbol{\tau}}} + \frac{\partial \bar{\mathbf{N}}}{\partial \bar{\boldsymbol{\tau}}} \Delta\gamma \right) & \underline{\underline{\mathbf{L}}}: \left(\bar{\mathbf{N}} \otimes \frac{\partial \Delta\gamma}{\partial \bar{\mathbf{B}}} + \frac{\partial \bar{\mathbf{N}}}{\partial \bar{\mathbf{B}}} \Delta\gamma \right) \\ -2\underline{\underline{\mathbf{P}}}: \left(\mathbf{b}^p \otimes \frac{\partial \Phi(I_1^p)}{\partial \bar{\boldsymbol{\tau}}} + \Phi(I_1^p) \frac{\partial \mathbf{b}^p}{\partial \bar{\boldsymbol{\tau}}} \right) & \mathbf{II} - 2\underline{\underline{\mathbf{P}}}: \left(\mathbf{b}^p \otimes \frac{\partial \Phi(I_1^p)}{\partial \bar{\mathbf{B}}} + \Phi(I_1^p) \frac{\partial \mathbf{b}^p}{\partial \bar{\mathbf{B}}} \right) \end{bmatrix}^{\alpha} \tag{41}$$

with $\Phi(I_1^p) = (\partial \Psi^p(I_1^p(\tau))) / \partial I_1^p$, and $\Delta\gamma = \Delta\gamma(\bar{\boldsymbol{\tau}}^{\alpha}(\tau), \bar{\mathbf{B}}'^{\alpha}(\tau))$, where the superscript α refers to the values at the end of the iteration procedure α . The derivatives in Eq. (41) are readily obtained, noting that both $I_1^p(\tau)$ and $\mathbf{b}^p(\tau)$ are functionally dependent on $\Delta\gamma$ which is a function of $\bar{\boldsymbol{\tau}}(\tau)$ and $\bar{\mathbf{B}}'(\tau)$ in terms of Eq. (24). From Eqs. (23) and (24), we have

$$\frac{\partial \Delta\gamma(\tau)}{\partial \bar{\boldsymbol{\tau}}} = \frac{\partial \Delta\gamma}{\partial \bar{\boldsymbol{\tau}}_{\text{eff}}} \cdot \frac{\partial \bar{\boldsymbol{\tau}}_{\text{eff}}}{\partial \bar{\boldsymbol{\tau}}} = \frac{\sqrt{2}}{2} \frac{\Delta\gamma(\tau)}{m \bar{\boldsymbol{\tau}}_{\text{eff}}^{\alpha}(\tau)} \bar{\mathbf{N}}^{\alpha}(\tau) \tag{42}$$

and

$$\frac{\partial \Delta\gamma(\tau)}{\partial \bar{\mathbf{B}}'} = \frac{\partial \Delta\gamma}{\partial \bar{\boldsymbol{\tau}}_{\text{eff}}} \cdot \frac{\partial \bar{\boldsymbol{\tau}}_{\text{eff}}}{\partial \bar{\mathbf{B}}'} = -\frac{\sqrt{2}}{2} \frac{\Delta\gamma(\tau)}{m \bar{\boldsymbol{\tau}}_{\text{eff}}^{\alpha}(\tau)} \bar{\mathbf{N}}^{\alpha}(\tau). \tag{43}$$

The derivatives of $\bar{\mathbf{N}}(\tau)$ with respect to $\bar{\boldsymbol{\tau}}(\tau)$ and $\bar{\mathbf{B}}'(\tau)$ take the form

$$\frac{\partial \bar{\mathbf{N}}(\tau)}{\partial \bar{\boldsymbol{\tau}}} = \frac{\underline{\underline{\mathbf{P}}} - \bar{\mathbf{N}}^{\alpha}(\tau) \otimes \bar{\mathbf{N}}^{\alpha}(\tau)}{\sqrt{2} \bar{\boldsymbol{\tau}}_{\text{eff}}^{\alpha}(\tau)} \tag{44}$$

and

$$\frac{\partial \bar{\mathbf{N}}}{\partial \bar{\mathbf{B}}'} = \frac{-\mathbf{II} + \bar{\mathbf{N}}^{\alpha}(\tau) \otimes \bar{\mathbf{N}}^{\alpha}(\tau)}{\sqrt{2} \bar{\boldsymbol{\tau}}_{\text{eff}}^{\alpha}(\tau)} \tag{45}$$

respectively. We have

$$\frac{\partial \Phi(I_1^p(\tau))}{\partial \bar{\boldsymbol{\tau}}} = \frac{\partial \Phi(I_1^p)}{\partial I_1^p} \frac{\partial I_1^p}{\partial \Delta\gamma} \cdot \frac{\partial \Delta\gamma}{\partial \bar{\boldsymbol{\tau}}} \tag{46}$$

and

$$\frac{\partial \Phi(I_1^p)}{\partial \bar{\mathbf{B}}'} = \frac{\partial \Phi(I_1^p)}{\partial I_1^p} \frac{\partial I_1^p}{\partial \Delta\gamma} \cdot \frac{\partial \Delta\gamma}{\partial \bar{\mathbf{B}}'}, \tag{47}$$

where the derivative of $I_1^p(\tau)$ with respect to $\Delta\gamma$ takes the form

$$\frac{\partial I_1^p(\tau)}{\partial \Delta\gamma} = 2\mathbf{I} : \left(\bar{\mathbf{N}}^z(\tau) \cdot \mathbf{b}^p(t) \cdot \left(\mathbf{I} + \Delta\gamma \bar{\mathbf{N}}^z(\tau) \right) \right). \tag{48}$$

In Eq. (41), the derivatives of $\mathbf{b}^p(\tau)$ with respect to $\bar{\boldsymbol{\tau}}$ and $\bar{\mathbf{B}}'$ take the form

$$\frac{\partial \mathbf{b}^p}{\partial \bar{\boldsymbol{\tau}}} = \frac{\partial \mathbf{b}^p}{\partial \Delta\gamma} \otimes \frac{\partial \Delta\gamma}{\partial \bar{\boldsymbol{\tau}}} \tag{49}$$

and

$$\frac{\partial \mathbf{b}^p}{\partial \bar{\mathbf{B}}'} = \frac{\partial \mathbf{b}^p}{\partial \Delta\gamma} \otimes \frac{\partial \Delta\gamma}{\partial \bar{\mathbf{B}}'}, \tag{50}$$

respectively, with

$$\frac{\partial \mathbf{b}^p(\tau)}{\partial \Delta\gamma} = \bar{\mathbf{N}}^z(\tau) \cdot \mathbf{b}^p(t) \cdot \left(\mathbf{I} + \Delta\gamma \bar{\mathbf{N}}^z(\tau) \right) + \left(\mathbf{I} + \Delta\gamma \bar{\mathbf{N}}^z(\tau) \right) \cdot \mathbf{b}^p(t) \cdot \bar{\mathbf{N}}^z(\tau). \tag{51}$$

After obtaining $\bar{\boldsymbol{\tau}}(\tau)$ and $\bar{\mathbf{B}}'(\tau)$ from solving Eq. (40), the plastic part of the deformation gradient, \mathbf{F}^p , is updated. The elastic part of the deformation gradient $\mathbf{F}^e(\tau) = \mathbf{F}(\tau) \cdot \mathbf{F}^p(\tau)^{-1}$ is then calculated. The interface traction defined in the reference configuration is obtained noting

$$\mathbf{T}(\tau) = \mathbf{P}(\tau) \cdot \mathbf{n}_0 = \mathbf{R}^e(\tau) \cdot \bar{\boldsymbol{\tau}}(\tau) \cdot \mathbf{R}^e(\tau)^T \cdot \mathbf{F}(\tau)^{-T} \cdot \mathbf{n}_0. \tag{52}$$

4.2. Linearization of interface virtual work

The tangent stiffness matrix of the interface element is obtained by the linearization of Eq. (4), which is expressed as

$$d(\delta W^{\text{INTER}}) = \int_{\Gamma_0} d\mathbf{P} \cdot \mathbf{n}_0 \cdot \delta \dot{\mathbf{A}} d\Gamma_0, \tag{53}$$

where $d\mathbf{P}$ takes the form

$$d\mathbf{P} = d\mathbf{R}^e \cdot \bar{\boldsymbol{\tau}} \cdot \mathbf{R}^{eT} \cdot \mathbf{F}^{-T} + \mathbf{R}^e \cdot d\bar{\boldsymbol{\tau}} \cdot \mathbf{R}^{eT} \cdot \mathbf{F}^{-T} + \mathbf{R}^e \cdot \bar{\boldsymbol{\tau}} \cdot d\mathbf{R}^{eT} \cdot \mathbf{F}^{-T} + \mathbf{R}^e \cdot \bar{\boldsymbol{\tau}} \cdot \mathbf{R}^{eT} \cdot d\mathbf{F}^{-T}. \tag{54}$$

To complete the linearization in Eq. (53), both $d\mathbf{R}^e$ and $d\bar{\boldsymbol{\tau}}$ need to be obtained. Combining Eqs. (34) and (35), we have

$$d\bar{\boldsymbol{\tau}}(\tau) = \underline{\underline{\mathbf{L}}} : d\bar{\mathbf{E}}_{\text{tr}}^e - \underline{\underline{\mathbf{L}}} : d[\Delta\gamma \bar{\mathbf{N}}(\tau)]. \tag{55}$$

After taking the derivatives, it is shown that Eq. (55) has the form

$$\underline{\underline{\mathbf{A}}} : d\bar{\boldsymbol{\tau}} = \underline{\underline{\mathbf{L}}} : d\bar{\mathbf{E}}_{\text{tr}}^e + \underline{\underline{\mathbf{L}}} : \left((\bar{\mathbf{N}} \otimes \bar{\mathbf{N}}) \frac{\sqrt{2}}{2} \frac{\Delta\gamma}{m\bar{\tau}_{\text{eff}}} - \frac{-\mathbf{II} + \bar{\mathbf{N}} \otimes \bar{\mathbf{N}}}{\sqrt{2}\bar{\tau}_{\text{eff}}} \Delta\gamma \right) : d\bar{\mathbf{B}}', \tag{56}$$

where

$$\underline{\underline{\mathbf{A}}} = \mathbf{II} + \underline{\underline{\mathbf{L}}} : (\bar{\mathbf{N}} \otimes \bar{\mathbf{N}}) \frac{\sqrt{2}}{2} \frac{\Delta\gamma}{m\bar{\tau}_{\text{eff}}} + \underline{\underline{\mathbf{L}}} : \frac{\mathbf{P} - \bar{\mathbf{N}} \otimes \bar{\mathbf{N}}}{\sqrt{2}\bar{\tau}_{\text{eff}}} \Delta\gamma. \tag{57}$$

The second term on the right-hand side of Eq. (56) is shown to be the same order as $(\Delta\gamma)^2$. For the sake of simplicity, this term was neglected in the calculations. As a result, we used a continuum tangent operator instead of a consistent tangent operator in the calculations conducted here. It is emphasized that the approximation may affect the convergence rate but not the accuracy. Eq. (56) is rewritten as

$$d\bar{\tau} \doteq \underline{\underline{A}}^{-1} : \underline{\underline{L}} : d\bar{\mathbf{E}}_{tr}^e, \tag{58}$$

where $\underline{\underline{A}}^{-1}$ is a fourth-order tensor which satisfies $\underline{\underline{A}}^{-1} : \underline{\underline{A}} = \mathbf{II}$. It is shown that $\underline{\underline{A}}^{-1}$ takes the form

$$\underline{\underline{A}}^{-1} = \frac{1}{1 + \beta_1} \mathbf{II} - \frac{\beta_2}{(1 + \beta_1)(1 + \beta_2 + \beta_1)} \bar{\mathbf{N}} \otimes \bar{\mathbf{N}} + \frac{\beta_1}{3(1 + \beta_1)} \mathbf{I} \otimes \mathbf{I}, \tag{59}$$

where $\beta_1 = \sqrt{2}\mu \frac{\Delta\gamma}{\bar{\tau}_{eff}}$ and $\beta_2 = \sqrt{2}\mu(\frac{1}{m} - 1) \frac{\Delta\gamma}{\bar{\tau}_{eff}}$. In the calculations conducted here, the differential $d\bar{\mathbf{E}}_{tr}^e$ takes the approximate form for the sake of simplicity

$$d\bar{\mathbf{E}}_{tr}^e \doteq \mathbf{R}_{tr}^{eT} d\mathbf{D}\mathbf{R}_{tr}^e, \tag{60}$$

where $d\mathbf{D} = \frac{1}{2}((\partial \mathbf{du}/\partial \mathbf{x}) + \partial^T \mathbf{du}/\partial \mathbf{x})$ with \mathbf{du} the displacement increment and \mathbf{x} the current position, and \mathbf{R}_{tr}^e is the trial elastic rotation tensor. In Eq. (54), the differential $d\mathbf{R}^e$ takes the form (Weber and Anand,1990)

$$d\mathbf{R}^e \doteq d\mathbf{F}_{tr}^e \mathbf{U}_{tr}^{e-1} - \mathbf{R}_{tr}^{eT} \text{sym}[\mathbf{U}_{tr}^{e-1} \text{sym}(\mathbf{F}_{tr}^{eT} d\mathbf{F}_{tr}^e)] \mathbf{U}_{tr}^{e-1}. \tag{61}$$

5. Parametric study of the interface model

In this section, the effects of material parameters characterizing the interface model are evaluated. For simplicity, a two-layer structure is modeled with a single 6-node interface element between two 6-node prism continuum elements. The 3D structure is described in Fig. 3. The thickness of each continuum element is $h/2$. Both simple shear and uniaxial tension in the direction tangential and perpendicular to the interface, respectively, are

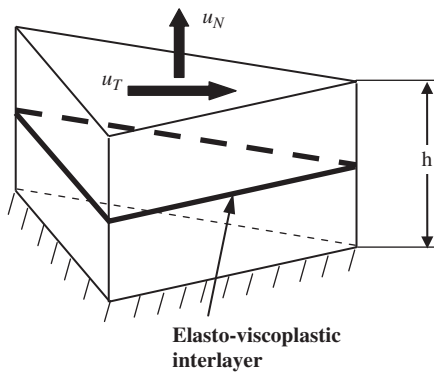


Fig. 3. Sketch of a two-layer composite material with the interface modeled by a 6-node interface element. Top and bottom layers are simulated by 6-node continuum elements. u_N and u_T denote the displacements in the direction perpendicular and parallel to the interface, respectively.

performed on the structure. In Fig. 3, u_N and u_T represent the displacements in the normal and tangential directions, respectively. Since the interface constitutive model is essentially isotropic, the material response under the simple shear condition is independent of the in-plane shear direction. In the calculations conducted here, a tablet thickness $h = 0.485 \mu\text{m}$ is used. Unless specified otherwise, the thickness of the interlayer is held fixed to $H = 0.035 \mu\text{m}$. The bulk material in the structure is taken to be purely elastic with the same transversely isotropic elastic constants as those for the mineral tablets of nacre. The five elastic constants are the Young’s modulus and Poisson ratio in the x – y symmetry plane, $E_P = 106 \text{ GPa}$ and $\nu_P = 0.3$, the Young’s modulus and Poisson ratio in the z -direction, $E_Z = 82 \text{ GPa}$ and $\nu_{ZP} = 0.06$, and the shear modulus in the z -direction, $G_{ZP} = 33.45 \text{ GPa}$ (Barthelat et al., 2006, 2007). An elastic shear modulus of $\mu = 1.0 \text{ GPa}$ is used for the interface material. The viscoplastic parameters used for the modeling include the reference shear rate $\dot{\gamma}_0 = 0.01$, and the rate sensitivity $m = 0.1$.

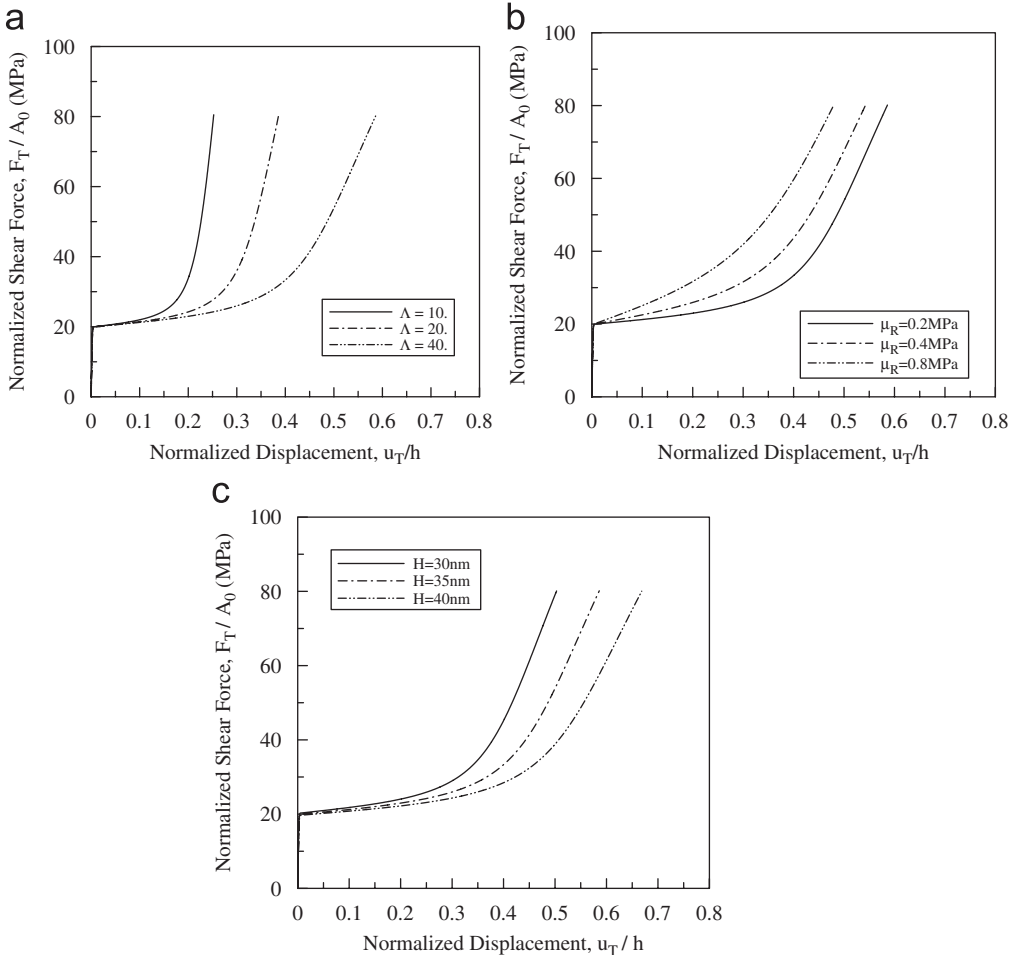


Fig. 4. Normalized shear force–displacement curves for (a) varying $\Lambda = L_c/p$ with $\mu_R = 0.2 \text{ MPa}$, (b) varying μ_R with $\Lambda = 40.0$, and (c) varying the interlayer thickness, H , with $\Lambda = 40.0$ and $\mu_R = 0.2 \text{ MPa}$.

5.1. Shear response

The effect of Λ , which is the ratio of the contour length to the persistence length in the WLC model, on the shear response of the structure is illustrated in Fig. 4(a). The displacement rate is taken to be $\dot{u}_T/h = 0.001 \text{ s}^{-1}$. In Fig. 4(a), the curves are plots of the shear force normalized by the undeformed interface area A_0 , i.e., $\tau_{sh} = F_T/A_0$, versus the normalized displacement, $\gamma_{sh} = u_T/h$, for $\Lambda = 10, 20$ and 40 . The hardening modulus, μ_R , is held fixed with a value of 0.2 MPa . As shown in Fig. 4(a), the flow resistance after yielding increases with the decrease of Λ . This is reasonable since a single wormlike chain is typically stiffer for a larger value of the persistence length. For an infinitely stiff wormlike chain, the persistence length is equal to its contour length. As the interface shear deformation increases such that the locking stretch, $\lambda_L = \sqrt{\Lambda/2}$, is approached, significant stiffening is observed. Fig. 4(b) illustrates the effects of μ_R on the interface behavior. The value of Λ is fixed at 40 in these calculations. The response curves for $\mu_R = 0.2, 0.4$ and 0.8 MPa are displayed. As expected, the shear strength increases with increasing μ_R . The normalized shear force–displacement curves for $H = 0.03, 0.035$ and $0.04 \text{ }\mu\text{m}$ are displayed in Fig. 4(c). As shown in this plot, the interlayer thickness plays an important role on the overall response of the structure under shear. The layered structure becomes stiffer with the decrease of the interlayer thickness. Furthermore, the shear displacement required for achieving locking decreases with decreasing interlayer thickness.

5.2. Tensile response

The tensile response of the layered composite subjected to uniaxial tension in the direction perpendicular to the interface is shown in Fig. 5. In this plot, the normalized

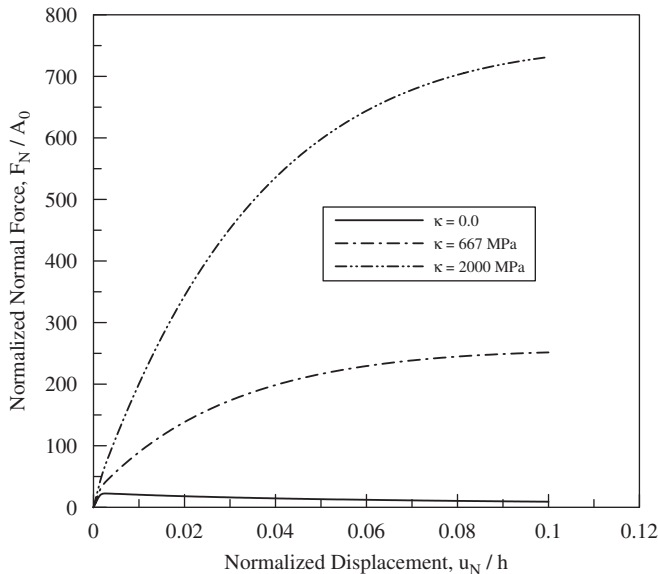


Fig. 5. Normalized normal force–displacement curves revealing the effects of the bulk modulus of the interface material on the material response when loaded in the direction perpendicular to the interface.

normal force–displacement curves for the elastic bulk modulus $\kappa = 2000, 1000$ and 0 MPa are displayed. It is shown that the bulk modulus plays an important role on the tensile response. With increasing bulk modulus, the tensile response curves exhibit a trend of increasing stiffness. This is related to the increase of stress triaxiality with the increase of bulk modulus. The interface material can become quite stiff as the inelastic deformation is suppressed in the presence of high stress triaxiality. In one of these three cases, we completely remove the stress triaxiality in the interface material by taking $\kappa = 0$. As indicated by the bottom curve in Fig. 5, the material response exhibits softening, feature not observed in the cases of non-zero bulk modulus.

6. Application to nacre

In this section, finite element simulations are performed on an RVE of nacre subjected to uniaxial tension. The RVE represents a two-phase composite of nacre consisting of mineral tablets embedded in an organic matrix. The organic material between tablets is simulated using the elasto-viscoplastic interface model discussed in the previous sections, while the tablets are assumed to be purely elastic with in-plane transverse isotropy. The finite element mesh used in this study is the same as that in Barthelat et al. (2006, 2007).

6.1. Finite element model for the RVE of nacre

In Fig. 6(a), the RVE in a 2D structure of nacre is indicated. In the modeling, the symmetry condition about the middle plane of the illustrated RVE under uniaxial tension

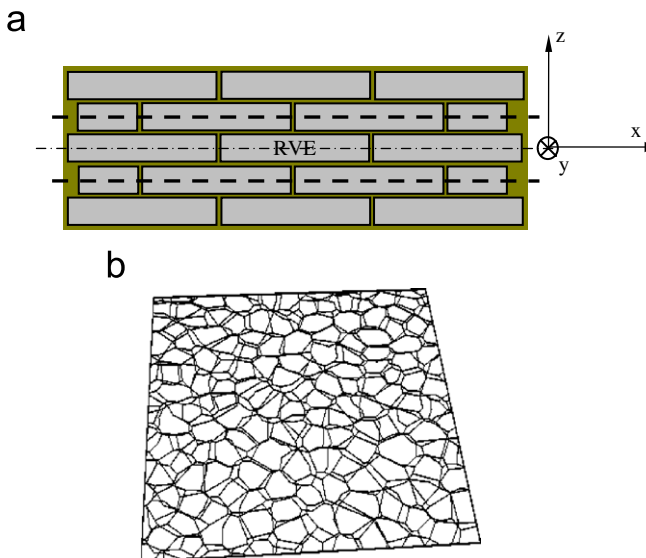


Fig. 6. (a) Sketch of the 2D structure of nacre. The RVE used in the simulations is indicated by the part between the dashed lines. Symmetry about the middle plane (x – y plane) is assumed during tension such that only one-half of the RVE needs to be modeled. (b) 3D RVE consisting of two layers of tablets, generated from the real structure of nacre. The tablets are modeled using continuum solid elements, and the interlayer is simulated using interface elements.

parallel to the x – y plane is assumed. As a result, only one half of the RVE needs to be modeled. As illustrated in Fig. 6(b), the finite element model of the RVE, consisting of two layers of tablets in half-thickness connected by the organic material, was directly generated from the real structure of nacre using image analysis techniques. The interface material is simulated using interface elements. More details on the generation of the finite element mesh were discussed by Barthelet et al. (2007). The plane area of the RVE is $72\ \mu\text{m} \times 78\ \mu\text{m}$ with a thickness of $0.485\ \mu\text{m}$. Each layer in the RVE contains over 150 tablets ensuring that the microstructure statistics of nacre are reflected in the simulations.

Periodic boundary conditions are imposed on the RVE. Accordingly, the tractions are opposite on opposite sides of the boundary of RVE, implying anti-periodicity, and the displacement on the boundaries has the form

$$\mathbf{u} = (\mathbf{F} - \mathbf{I})\mathbf{X} + \tilde{\mathbf{u}}, \tag{62}$$

where \mathbf{u} is the boundary displacement corresponding to position \mathbf{X} ,

$$\bar{\mathbf{F}} = \frac{1}{V_0} \int_{B_0} \mathbf{F} \, dV$$

is the volume average of the deformation gradient, \mathbf{F} , over the undeformed configuration B_0 , and $\tilde{\mathbf{u}}$ is the disturbance of boundary displacement, which is periodic. It is easy to show that

$$\bar{\mathbf{P}} : \dot{\bar{\mathbf{F}}} = \frac{1}{V_0} \int_{B_0} \mathbf{P} : \dot{\mathbf{F}} \, dV, \tag{63}$$

where

$$\bar{\mathbf{P}} = \frac{1}{V_0} \int_{B_0} \mathbf{P} \, dV$$

is the volume average of the first Piola–Kirchhoff stress over the undeformed configuration, under periodic boundary conditions. The terms, $\dot{\bar{\mathbf{F}}}$ and $\dot{\mathbf{F}}$, denote the rates of $\bar{\mathbf{F}}$ and \mathbf{F} , respectively. This implies that $\bar{\mathbf{P}}$ is work conjugate with $\bar{\mathbf{F}}$. The macroscopic Cauchy stress or overall stress is defined by $\bar{\boldsymbol{\sigma}} = \bar{\mathbf{P}}\bar{\mathbf{F}}^T / \bar{\mathcal{J}}$ with $\bar{\mathcal{J}} = \det \bar{\mathbf{F}}$. In the finite element analysis, the periodic boundary conditions are expressed by using the constraint

$$\mathbf{u}^A - \mathbf{u}^B = (\bar{\mathbf{F}} - \mathbf{I})(\mathbf{X}^A - \mathbf{X}^B), \tag{64}$$

where \mathbf{u}^A and \mathbf{u}^B denote boundary displacements at two periodic image boundary positions \mathbf{X}^A and \mathbf{X}^B , respectively.

We simulate the deformation of the RVE under uniaxial tension conditions by applying the time-dependent deformation gradient

$$\bar{\mathbf{F}}(\mathbf{t}) = \bar{\lambda}_1(\mathbf{t})\mathbf{e}_1 \otimes \mathbf{e}_1 + \bar{\lambda}_2(\mathbf{t})\mathbf{e}_2 \otimes \mathbf{e}_2 + \bar{\lambda}_3(\mathbf{t})\mathbf{e}_3 \otimes \mathbf{e}_3, \tag{65}$$

where \mathbf{e}_1 , \mathbf{e}_2 and \mathbf{e}_3 are Cartesian basis vectors, and $\bar{\lambda}_i|_{i=1,3}$ are macroscopic principal stretches. Initial conditions are $\bar{\mathbf{F}} = \mathbf{I}$, with \mathbf{I} the identity tensor, at $t = 0$, corresponding to the undeformed state. We take $\bar{\lambda}_{1(2)}(\mathbf{t}) = \exp(\dot{\epsilon}t)$, with $\dot{\epsilon}$ the applied strain rate, while $\bar{\lambda}_{2(1)}$ and $\bar{\lambda}_3$ are left free, corresponding to the uniaxial tension in the $\mathbf{X}_1(\mathbf{X}_2)$ direction.

6.2. Rate-independent interface damage model

Under tension parallel to the tablet plane (x – y plane), the organic material between vertical walls at tablet junctions has to sustain much larger tensile deformation than that between tablet planes. Due to strong constraints to the tensile deformation of the organic material, as imposed by the tablets, high stress triaxiality arises in the organic interlayer. This is responsible for ligament formation and fibril breakage. These damage effects are not included in the present elasto-viscoplastic interface model. Hence, to account for this effect the organic material between vertical walls at tablet junctions is modeled using a phenomenological irreversible cohesive law (Barthelat et al., 2007).

The interface material between the vertical walls at tablet junctions is assumed to resist both opening and sliding of tablets. We define the interface traction as

$$\mathbf{T} = \frac{\Delta}{\Delta^{\text{eff}}} T^{\text{eff}}, \quad (66)$$

where $\Delta^{\text{eff}} = \sqrt{\Delta \cdot \bar{\Delta}}$ is the effective displacement jump, and T^{eff} is the effective interface traction. Here T^{eff} is taken to have the forms

$$T^{\text{eff}} = \frac{\Delta^{\text{eff}}}{\delta_{c1}} T^{\text{max}}, \quad \Delta^{\text{eff}} \leq \delta_{c1}, \quad (67)$$

$$\begin{cases} T^{\text{eff}} = T^{\text{max}}, & \delta_{c2} \geq \Delta^{\text{eff}} > \Delta_{\text{max}}^{\text{eff}} \geq \delta_{c1}, \\ T^{\text{eff}} = T^{\text{max}} \frac{\Delta^{\text{eff}}}{\Delta_{\text{max}}^{\text{eff}}}, & \delta_{c2} \geq \Delta_{\text{max}}^{\text{eff}} > \Delta^{\text{eff}} \end{cases} \quad (68)$$

and

$$\begin{cases} T^{\text{eff}} = \frac{\delta_c - \Delta^{\text{eff}}}{\delta_c - \delta_{c2}} T^{\text{max}}, & \delta_c > \Delta^{\text{eff}} > \Delta_{\text{max}}^{\text{eff}} > \delta_{c2}, \\ T^{\text{eff}} = \left(1 - \frac{\Delta_{\text{max}}^{\text{eff}}}{\delta_c}\right) T^{\text{max}} \frac{\Delta^{\text{eff}}}{\Delta_{\text{max}}^{\text{eff}}}, & \delta_c > \Delta_{\text{max}}^{\text{eff}} > \Delta^{\text{eff}}, \end{cases} \quad (69)$$

where δ_{c1} , δ_{c2} and δ_c are the characteristic opening displacements, and T^{max} is the maximum effective traction as indicated in Fig. 7. The variable $\Delta_{\text{max}}^{\text{eff}}$ is a state variable tracking the maximum achieved opening displacement. According to Eqs. (66)–(69), damage effects are included after $\Delta^{\text{eff}} > \delta_{c1}$. As described in Fig. 7, both the effective traction and the opening displacement tend to return to the origin along a linear path in the presence of unloading. In the simulations we use $T^{\text{max}} = 20$ MPa, $\delta_c = 600$ nm, $\delta_{c1} = 0.36$ nm, and $\delta_{c2} = 270$ nm (Barthelat et al., 2007). For a justification on the choice of these parameters see Barthelat et al. (2007).

6.3. Parameters characterizing the elasto-viscoplastic interface model

In the WLC model, one of the important parameters controlling the stiffening behavior of a single polymer chain is the ratio of the contour length to the persistence length, $A = L_c/p$. Progressive unfolding of proteins in the organic material of nacre is expected. As a result, the contour length, L_c , typically evolves with increasing length. To a first

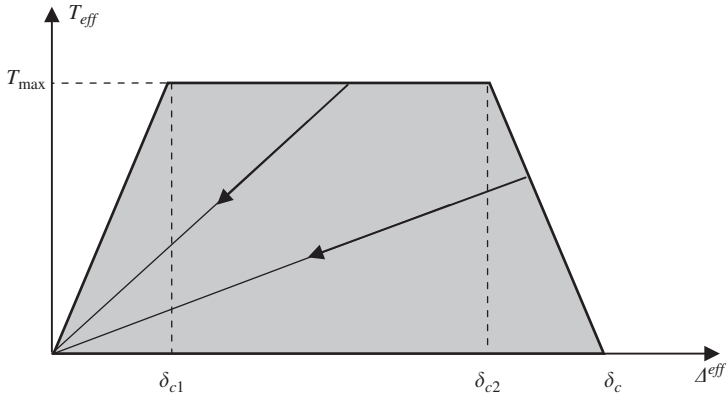


Fig. 7. Sketch showing the constitutive relationship between the effective interface traction and the effective displacement jump for a rate-independent damage model.

approximation, the unfolding mechanism is not included in the present interface model but its effect is investigated parametrically. From the experimentally obtained force–extension curves for the organic material of nacre (Smith et al., 1999), it is estimated that the initial contour length corresponding to the occurrence of the first unfolding of a protein chain is about 16 nm. The persistent length is taken to be $p = 0.4$ nm (Qi et al., 2005). Hence, the value of $\lambda = L_c/p$ for the protein chain in the organic material of nacre is estimated to be at least 40. The hardening modulus $\mu_R = nk\theta$ in the WLC model (Eq. (30)) was fitted to experimentally measured tensile stress–strain curves.

The parameters characterizing the elastic properties of the organic material are the shear modulus, μ , and the bulk modulus, κ . A value of 1.4 GPa was reported by Jackson et al., (1988) for the shear modulus of the wet organic matrix; while 0.8 GPa was reported by Barthelat et al. (2006, 2007). In the calculations conducted here, the shear modulus was taken to have a value of 1.0 GPa between these two reported values. As stated earlier, the elastic bulk modulus can play a significant role on the interface behavior of nacre due to the confinement of the thin layer between relative rigid mineral tablets. SEM images (Jackson et al., 1988) revealed that the organic material forms ligaments bridging mineral tablets. Here, we assume that ligament formation reduces the hydrostatic stresses created by the strong confinement in the thin interlayer. This is incorporated in the simulations here reported by using a bulk modulus of 400 MPa unless otherwise specified. This value was identified by fitting the experimental data for uniaxial tension. The viscoplastic material properties for the organic material are the reference shear rate $\dot{\gamma}_0 = 0.01$ s⁻¹, the rate sensitivity $m = 0.1$, reasonable for a rate sensitive material, and the yield strength $s = 20$ MPa. The value of s was obtained by fitting the experimental tensile stress–strain curve. We summarize the parameters characterizing the elasto-viscoplastic interface model in Table 1. In addition, the strain rate was taken to be $\dot{\epsilon} = 0.1\%$ s⁻¹. Unless otherwise stated, these values are used in the calculations conducted here.

6.4. Tablet climbing in the presence of surface waviness

As shown in Fig. 8, the surface topology of the interface can play a significant role on the material response of the interlayer between tablets. In Figs. 8(a) and (c), the initial

Table 1
Parameters characterizing the elasto-viscoplastic interface model of nacre

μ (GPa)	S (MPa)	μ_R (MPa)	H (nm)	A	$\dot{\gamma}_0$ (s^{-1})	m
1.0	20.0	0.2	35	40.0	0.01	0.1

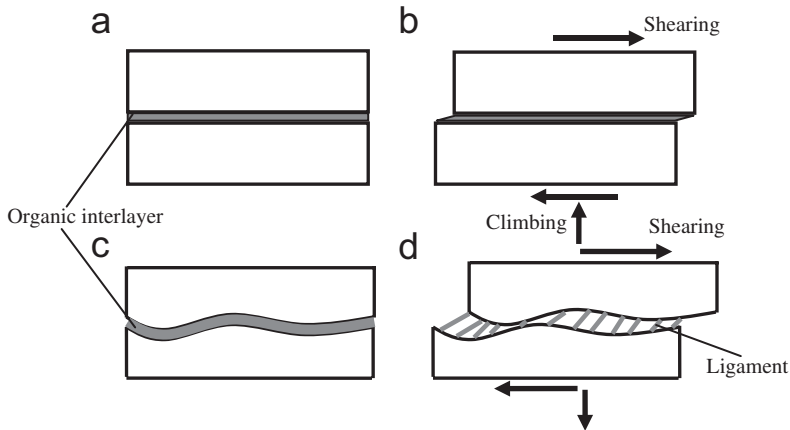


Fig. 8. Schematic configurations showing the deformation behavior of the organic interlayer during the relative sliding between tablets for cases with and without surface waviness: (a) the initial configuration without waviness; (b) the configuration under shear without waviness; (c) the initial configuration with waviness; (d) the configuration under shear with waviness. Tablet climbing is displayed in the case with interface waviness. Due to the constrained tensile response illustrated in (d), the interface material bridges the tablets through formation of ligaments.

configurations of two overlapped tablets connected by the interlayer material are displayed. Comparing Figs. 8(b) and (d), it is seen that the deformation behavior of the interface material during the relative sliding of tablets in the presence of waviness differs significantly from that in the absence of waviness (flat interfaces). In the former, the relative sliding between tablets leads to the simple interface shear as described in Fig. 8(b). This is in direct contrast to the latter as shown in Fig. 8(d). In this case, interface shearing is locally coupled to tension or compression. As a consequence of the strong confinement of the thin interlayer, the tensile deformation is constrained. In fact, the organic interface material can become very stiff as previously illustrated in Fig. 5. Experimentally, it has been observed that the organic material develops ligaments (Jackson et al., 1988; Smith et al., 1999) releasing high stress triaxiality and enhancing the toughness of nacre. The ligaments contain a large number of protein fibrils which have been shown to be very stretchable (Jackson et al., 1988; Smith et al., 1999). Crack bridging associated with ligament elongation is believed to be an important mechanism leading to the high level of toughness of nacre (Sarikaya et al., 1990, 1992). Certainly, from the viewpoint of an analysis of the local interface response, such effect is quite relevant.

In Fig. 9, the surface tractions acting on a nacre tablet sliding to the left are illustrated. As shown in this plot, the force, F_c , arising from the compression of the tablets in the presence of surface waviness, contributes to tablet climbing. This force must be balanced

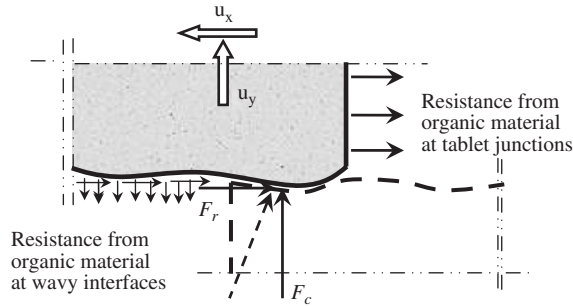


Fig. 9. Diagram illustrating the distribution of local tractions and forces on the surface of a sliding tablet. Both the organic material and the surface waviness provide resistances to the relative sliding between tablets. The interface material imposes constraints to both tablet sliding and tablet climbing. F_r and F_c denote the horizontal and vertical forces, respectively acting on the top tablet as a result of local compression of the wavy interface.

by the stretching of the organic material in other regions of the interface. Here, the organic material plays a significant role in constraining tablet climbing, thereby increasing the resistance to the overall deformation. The various contributions to tablet sliding resistance are summarized in Fig. 9. These are the shear traction arising from the shearing of the organic material at interface between tablets, and the force, F_r , arising from tablet compression in the presence of waviness. The stretching of the organic material at the tablet junctions provides additional resistance to tensile deformation. All these contributions are responsible for the strength macroscopically exhibited by nacre.

The climbing of tablets was revealed experimentally by the transverse expansion exhibited in the shear testing of nacre specimens (Barthelat et al., 2006, 2007). The transverse expansion was also captured in the simulated shear response of the nacre RVE. In Fig. 10, the curves of transverse strain-shear strain with varying Δ_{cr} are displayed and compared to the experimental data. An increase in Δ_{cr} corresponds to an increased interface compliance. The climbing of tablets starts as the compression of the organic interlayer becomes significant. As shown in Fig. 10, the simulation predicts a progressive increase in transverse strain with increasing shear strain beyond a threshold of about 2–3%. The experimental data shows a detectable transverse contraction followed by a transverse expansion beyond a threshold shear strain. This is consistent with the occurrence of significant tablet climbing as discussed in the previous paragraph. From this discussion one can conclude that for $\Delta_{cr} = 0.05H$, the simulation results are in good agreement with the experimental data in capturing sliding-induced dilation. This value is therefore used in all the calculations discussed in subsequent sections.

6.5. Tensile response of nacre

6.5.1. Comparison with experimental data for uniaxial tension

Since nacre is expected to behave transversely isotropically we begin by loading the RVE in the x , y and 45° directions, as illustrated by the inset shown in Fig. 11. In this figure, we compare the predicted tensile response curves in these three directions with the experimental data reported in Barthelat et al. (2006, 2007). It is noted that similar response curves are obtained for these three loading directions. The small differences

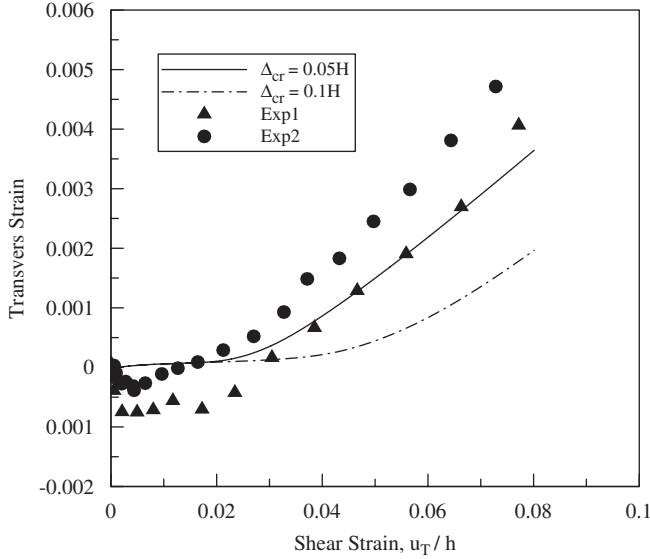


Fig. 10. Curves of transverse strain versus shear strain for $\Delta_{cr} = 0.05H$ and $0.1H$. The experimental data from two shear tests (Barthelat et al., 2006, 2007) are displayed for comparison. Tablet climbing is revealed by the transverse expansion.

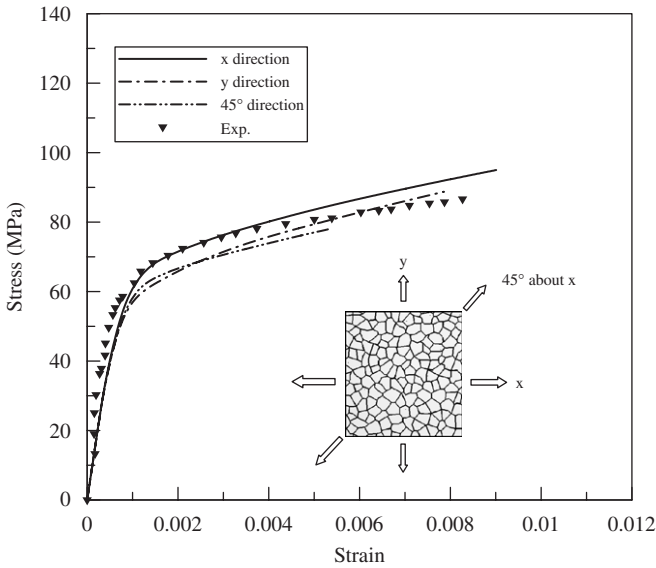


Fig. 11. Macroscopic stress–strain curves for three different tensile loading directions as indicated by the inset. The experimental data is also displayed for comparison.

between them imply that the size of the RVE used in the simulations is not sufficiently large to fully capture the transverse isotropy. However, due to the computational cost and the small differences in the results, larger RVEs were not investigated.

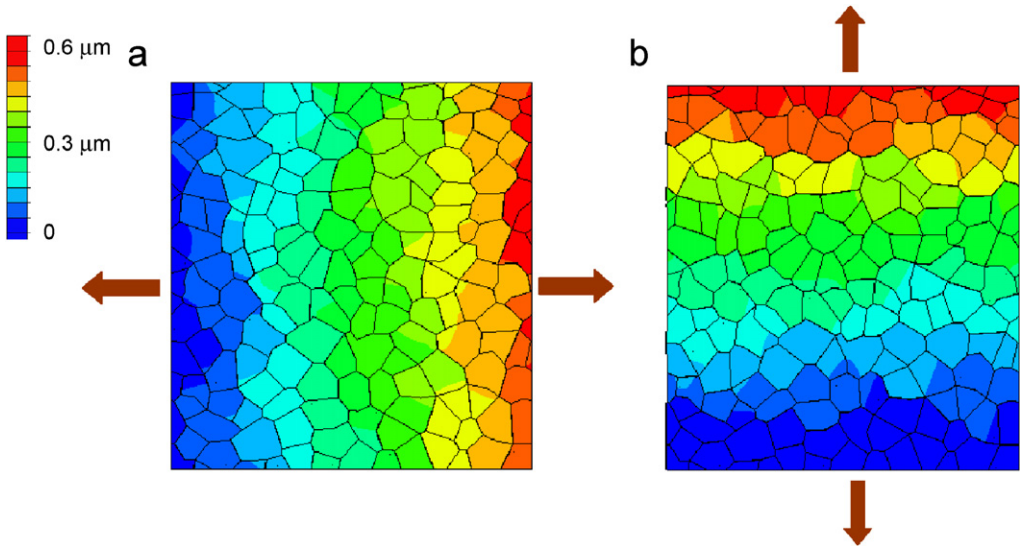


Fig. 12. Contour plots of the displacements (a) u_x and (b) u_y for the RVE of nacre subjected to uniaxial tension in the x and y directions, respectively. The overall tensile strain is 0.72%.

In Fig. 11, the initial yield behavior is characterized by a rounded shape. Such shape is an outcome of the tablet overlap statistics. Also observed in Fig. 11 is the noticeable strain hardening with increased tensile deformation. As discussed in Barthelat et al. (2006, 2007), this plays a crucial role in preventing localized tensile deformation leading to relatively large strains. Indeed, according to experiments and RVE simulations, the deformation of nacre under uniaxial tension is quite uniform. In the calculations here discussed this is illustrated in Figs. 12(a) and (b), which show contour plots of displacements, u_x and u_y , at 0.72% overall strain, for the nacre RVE loaded in the x and y directions, respectively. As shown in Figs. 12, the displacement varies smoothly through the segmented layer. This is directly related to the hardening behavior exhibited by nacre. The uniform deformation behavior of the nacre RVE is further revealed by the distribution of the normal stress in the x direction as shown in Fig. 13. In this contour plot, the load is shown to be well distributed over the RVE consistent with tablet organization. At a strain of 0.72% the average normal stress in the x -direction is about 80 MPa. The plot shows local stresses higher and lower than the average consistent with tablet overlap distribution.

In Fig. 9, we illustrate the effect of tablet climbing during tensile deformation and associated out-of-plane normal stress distribution on the waved surfaces. Such distribution of the out-of-plane normal stress, in the direction perpendicular to the tablet planes, is plotted in Fig. 14. A salient feature of the out-of-plane stress distribution is that compressive stresses emerge in many areas near tablet junctions, where significant interface shearing occurs. The compressive stresses are generated when the top tablets climb over the bottom ones in the presence of waviness. As shown in Fig. 14, tensile stresses typically appear in the middle of the tables, which were denoted as core areas in Barthelat et al. (2007). The tensile stresses arise from the stretching of the organic material to balance the climbing contact forces. Noting the relatively large surface areas of the tablets, a small tensile stress developed in the organic material can lead to strong constraints to tablet

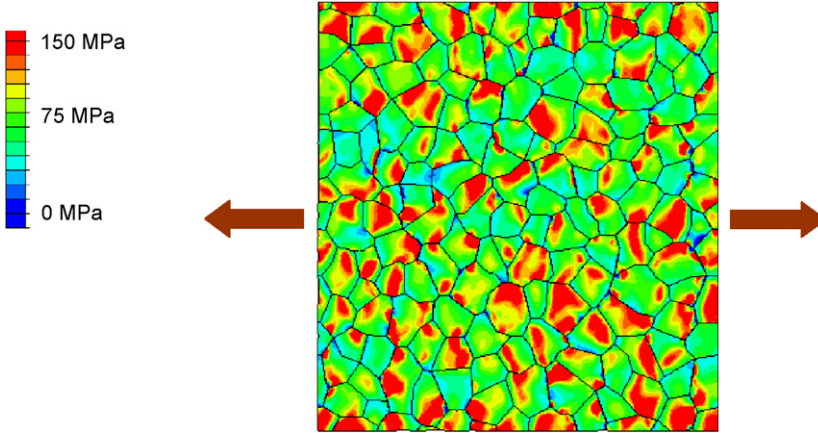


Fig. 13. Contour plot of the normal stress, σ_{xx} , for the RVE subjected to uniaxial tension in the x direction at 0.72% overall tensile strain.

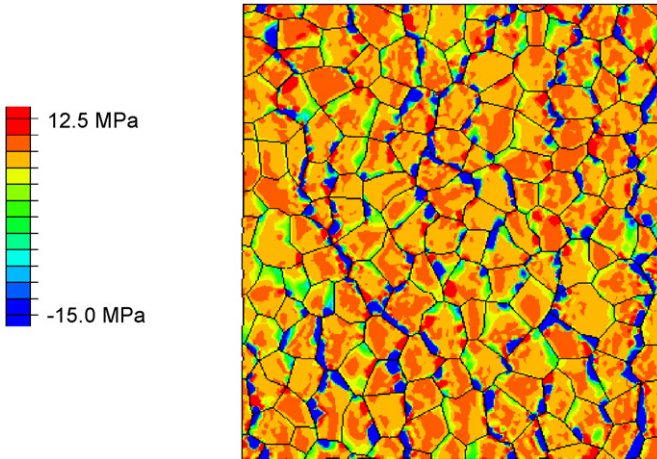


Fig. 14. Contour plot of the out-of-plane normal stress, σ_{zz} , at 0.72% overall tensile strain. The compressive stress near the tablet junctions where significant relative sliding occurs is evident.

climbing. This is important for the strengthening of nacre. A similar plot as Fig. 14 was also obtained using the non-hardening traction-separation law in Barthelat et al. (2006, 2007). This implies that the features revealed in Fig. 14 are mainly structure related.

6.5.2. Effects of the bulk modulus of the organic material on the tensile response

The constrained transverse expansion associated with the relative sliding between tablets can induce significant stress triaxiality depending on the bulk modulus of the organic material. In Fig. 15, the effect of the bulk modulus, κ , on the tensile response of the nacre RVE subjected to uniaxial tension in the x direction is illustrated. As shown in the plot, the predicted hardening rate for the nacre RVE increases with increasing bulk modulus. This implies that the constraint to tablet climbing becomes stronger with increasing bulk modulus, thereby increasing the hardening rate. The lowest curve in Fig. 15 also

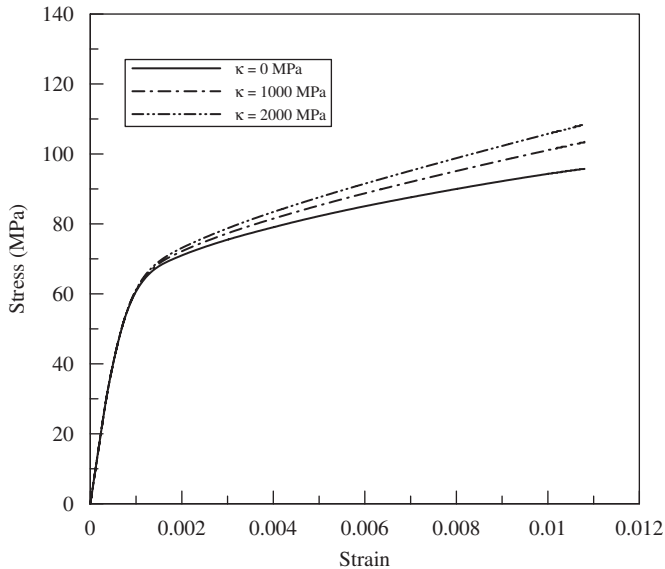


Fig. 15. Effect of bulk modulus on macroscopic tensile stress–strain response. RVE is subjected to uniaxial tension.

corresponds to $\kappa = 0$. In this case, the effects of confinement on the thin interlayer can be significantly reduced as previously discussed in relation to Fig. 5. Note that the change in hardening rate is moderate taking into account that k has been varied over a decade.

6.5.3. Strain-rate dependence of the tensile response

The strain-rate dependence of nacre was experimentally revealed in Menig et al. (2000). The present elasto-viscoplastic interface model accounts for the strain-rate dependence through the power-law relationship as described by Eq. (24). Here, we do not attempt to capture the physical basis for the rate-dependent behavior of nacre, but instead demonstrate that the present interface model is capable of capturing rate-dependence. We simulated the tensile responses of the nacre RVE at various strain rates $\dot{\epsilon}/\dot{\gamma}_0 = 0.1, 1.0$ and 10. The predicted stress–strain curves are plotted in Fig. 16. In the corresponding calculations, the RVE of nacre is subjected to uniaxial tension in the x direction with $\lambda_1(t) = \exp(\dot{\epsilon}t)$. As shown in Fig. 16, the flow stresses is shown to increase with the increase of the applied strain rates. The strain-rate dependence is totally attributed to the viscoplastic deformation of the organic material. It is interesting to note that while only a very small proportion of the biocomposite is organic material, it dominates the overall mechanical behavior of nacre. This is attributed to the mechanism of load transfer in the biocomposite. The organic material accommodates most of the inelastic deformation in nacre through tablet shearing, dissipating energy through viscoplastic shearing and stretching.

6.5.4. Loading cycles

To further demonstrate the predictive capability of the present interface model, we simulated the mechanical behavior of nacre during consecutive loading, unloading and reloading. In the simulations, the RVE was subjected to uniaxial tension in the x direction.

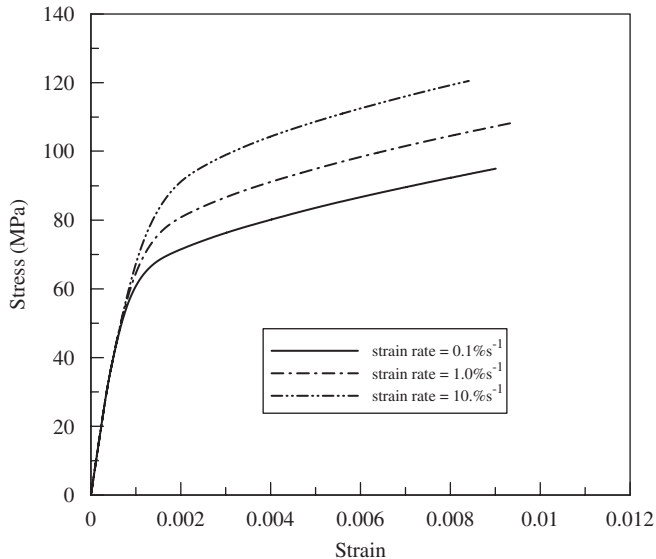


Fig. 16. Effect of strain rate on macroscopic tensile stress–strain response. RVE is subjected to uniaxial tension at various deformation rates.

At 0.4% overall strain, the RVE was unloaded until the macroscopic overall stress became zero. Then the RVE was reloaded at the same strain rate to an overall strain of 0.8%. Following this loading step, the RVE was unloaded again until the macroscopic stress was completely released. Reloading of the RVE was performed following the unloading step. Thereafter, two unloading–reloading cycles at different strain levels were obtained. As shown in Fig. 17, hysteresis loops are predicted in the tensile stress–strain curve. We note that hysteresis loops were also experimentally observed in tensile tests performed on nacre specimens by Currey (1977). However, the underlying mechanisms can be better understood through the simulation results here presented. The areas enclosed by the hysteresis loops increase with increasing deformation, indicative of increased energy dissipation during the unloading–reloading cycles. Fig. 17 shows that the unloading is not purely elastic. This implies that significant viscoplastic deformation occurs in the interface material during unloading. The elastic–plastic interactions between the organic matrix and mineral tablets appear to prevent the unloading being fully elastic. The mineral tablets are purely elastic tending to totally recover from deformation with unloading. However, the recovering is subjected to constraints from the surrounding organic material which has undergone significant viscoplastic deformation.

The tensile tests of nacre performed by Currey (1977) showed that, upon reloading a plastically deformed specimen, the elastic modulus was less than the previously measured elastic modulus. This was attributed to the accumulated damage in the organic material with the increase of inelastic deformation. Damage in nacre is related to the formation of ligaments and chain breakage in the organic material. In Fig. 17, damage effects on decreasing the elastic modulus are not clearly revealed, although a rate-independent interface damage model is used to model the interface material between tablet junctions. This shows that the damage effects in the organic material between tablet planes need to be properly accounted for in the elasto-viscoplastic interface model to capture the

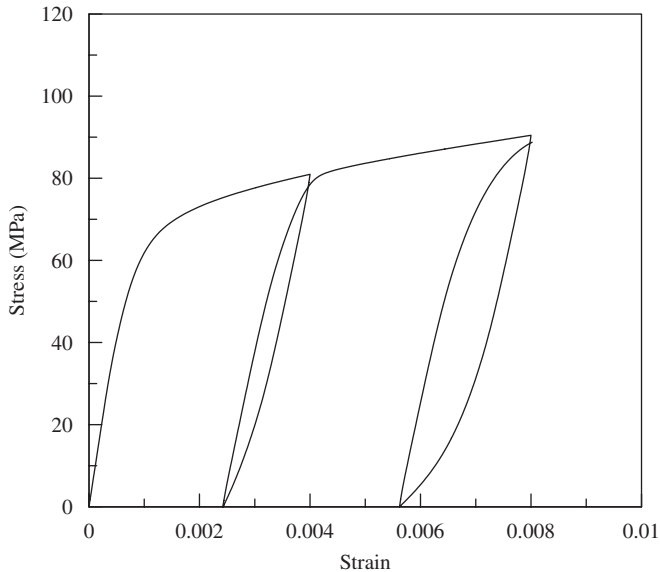


Fig. 17. Predicted macroscopic stress–strain response for a nacre RVE undergoing consecutive loading, unloading and reloading cycles. Hysteresis loops are predicted by the simulations.

experimental measured decrease in elastic modulus with increasing deformation. In future studies, a stress-state dependent damage variable could be included in the elasto-viscoplastic interface model to simulate damage effects. Such effort is beyond the scope of the present investigation.

6.5.5. Effects of the ratio of the contour length to the persistence length

The organic material in nacre is expected to become significantly stiff as biopolymer chains approach full extension, thereby leading to a concave upward hardening behavior. This is typical in the deformation of polymer materials. However, such hardening behavior was not exhibited in the tensile tests of nacre. The reasons for such behavior are here discussed. In Fig. 18, the predicted tensile response curves for the nacre RVE subjected to uniaxial tension in the x direction are displayed for various values of λ . The upward hardening behavior is clearly predicted for $\lambda = 3$. Nonetheless, in this case the predicted tensile response is significantly stiffer than the one experimentally measured. As λ becomes greater than 40, the predicted tensile response tends to be insensitive to the increase of λ in the strain range from 0% to 1.5%. Indeed, the tensile response for λ greater than 40 differs slightly from that without including back stress or the stiffening of polymer in the modeling. Furthermore, the predicted tensile response in the absence of a back stress agrees well with the experimentally obtained data as shown in Fig. 18. As discussed in Section 6.3 in the context of protein pull-out experiments, the ratio of contour length to persistence length, λ , for proteins typically encountered in the organic material of nacre, appears to be larger than 40. These results clearly show that polymer stiffening is not required for the hardening of nacre in tension. This finding supports the phenomenological cohesive law used in the simulations reported in Barthelat et al. (2007).

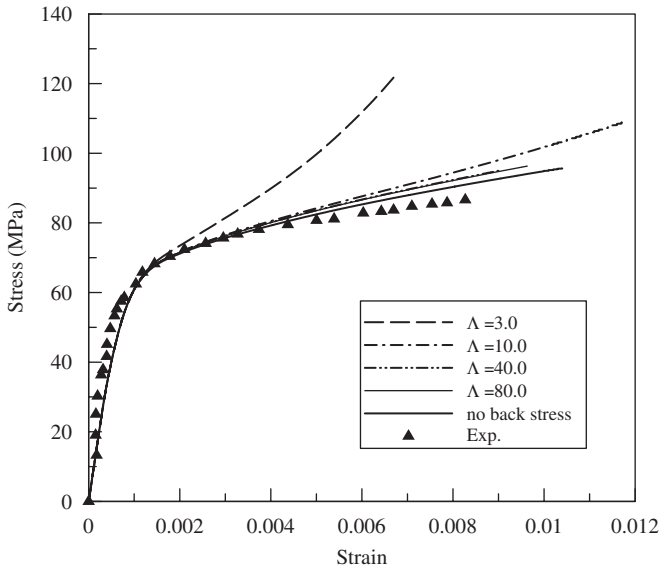


Fig. 18. Macroscopic tensile stress–strain curves as a function of λ . The curve for the case omitting the back stress (absence of polymer stiffening) is plotted for comparison.

The hardening behavior of nacre in tension turns out to be structure related. The interface waviness-related climbing mechanism is believed to hold the key to such hardening behavior. A crucial role that the organic material plays is to constrain the climbing of tablets associated with inter-tablet shearing in the presence of surface waviness. This can significantly increase the resistance to tablet sliding and strengthen the material. The polymer contribution to the strengthening of nacre is indeed enhanced in the presence of surface waviness in the sense that tablet climbing induces additional stretching of the organic material in the direction normal to the interface.

7. Concluding remarks

In this paper, we derived and implemented an elasto-viscoplastic interface model to simulate the constitutive behavior of the organic material in nacre. The developed interface model accounts for the elasto-viscoplastic response of the organic material in a unified manner. The single biopolymer chain behavior is characterized by the WLC model, which is incorporated into the macroscopic constitutive description for the organic material through the Arruda–Boyce 8-chain model. Compared with conventional interface models in which the specified interface laws are phenomenological, the interface model presented here is more physically motivated because it takes into account the relevant micromechanisms controlling the interface material deformation. In this context, the interface model was developed to characterize the mechanical behavior of the organic material in nacre to gain insight into the mechanisms leading to the exceptional properties exhibited by this material. However, it is emphasized that the model is versatile and particularly suited for modeling the rate-dependent mechanical behavior of a wide range of interface materials.

The elasto-viscoplastic interface model was formulated within a finite-deformation framework. This was necessary in order to account for the significant local shearing and stretching undergone by the interface material. In solving the incremental constitutive equations associated with the interface model, a fully implicit time-integration procedure was implemented based on the conventional Newton–Raphson method. The local Jacobian matrix for the Newton–Raphson scheme was calculated in closed form taking into account the couplings of all constitutive equations. This resulted in a robust, stable, efficient and accurate algorithm for the computations. While an approximate form of element stiffness matrix was formulated for simplicity, the convergence rate for solving the global equilibrium equations was found to be acceptable.

The capability of the elasto-viscoplastic interface model in predicting the material response of nacre subjected to uniaxial tension is demonstrated in this paper. The finite element simulations were performed on an RVE of nacre with periodic boundary conditions imposed. The finite element model was generated from experimentally obtained microstructural features. In particular, the surface topology at the interface was taken into account in the simulations.

By means of the developed interface model, we show that the back stress arising from the plastic stretch of the organic material plays a trivial role on the hardening behavior of nacre during tension. This is reasonable noting the large locking stretch of polymeric fibrils in the organic material as identified by SEM and AFM studies. Therefore, a structure-related hardening mechanism (Barthelat et al., 2007) is further confirmed. The mechanism is related to the local climbing of tablets in the presence of surface waviness. Both the resistance to tablet sliding due to waviness and the constrained transverse expansion leading to organic stretching appear to hold the key to the hardening behavior of nacre.

Modeling the material response in tension during consecutive loading, unloading and reloading cycles revealed the existence of hysteresis loops. The size of the loops increases with increasing plastic deformation. This is qualitatively consistent with experimental observations in the testing of nacre. However, the experimentally observed damage effects reflected by the decrease of reloading elastic modulus are not captured by the present elasto-viscoplastic interface model. An augmented model with damage variables needs to be developed to model damage in the organic interlayer and its effect on the overall mechanical behavior of nacre.

Acknowledgments

This research was supported by the National Science Foundation through award No. CMS-0301416 and the US Army Research Office through Grant no. W911NF-05-1-0088. Computing support from the San Diego Supercomputer Center is gratefully acknowledged. We would like to thank Dr. Amit Acharya for helpful discussions on numerical methods used in this research.

References

- ABAQUS, 2004. ABAQUS Reference Manuals. Hibbit, Larlsson and Sorensen Inc., Pawtucket, RI.
- Anand, L., Gurtin, M.E., 2003. A theory of amorphous solids undergoing large deformation. *Int. J. Plasticity* 9, 1465–1487.

- Arruda, E.M., Boyce, M.C., 1993a. A three-dimensional constitutive model for the large stretches, with application to polymeric glasses. *Int. J. Solids Struct.* 40, 389–412.
- Arruda, E.M., Boyce, M.C., 1993b. Evolution of plastic anisotropy in amorphous polymers during finite straining. *Int. J. Plasticity* 9, 697–720.
- Bao, G., Suresh, S., 2003. Cell and molecular mechanics of biological materials. *Nat. Mater.* 2, 715–725.
- Barthelat, F., Li, C.M., Comi, C., Espinosa, H.D., 2006. Mechanical properties of nacre constituents and their impact on mechanical performance. *J. Mater. Res.* 21 (8), 1977–1986.
- Barthelat, F., Tang, H., Zavattieri, P.D., Li, C.-M., Espinosa, H.D., 2007. On the mechanics of mother-of-pearl: a key feature in the material hierarchical structure. *J. Mech. Phys. Solids* 55 (2), 306–337.
- Bischoff, J.E., Arruda, E.M., Grosh, K., 2002. Orthotropic hyperelasticity in terms of an arbitrary molecular chain model. *J. Appl. Mech.* 69, 199–201.
- Camacho, G.T., Ortiz, M., 1996. Computational modeling of impact damage in brittle materials. *Int. J. Solids Struct.* 33, 2899–2938.
- Currey, J.D., 1977. Mechanical properties of mother of pearl in tension. *Proc. R. Soc. London* 196, 443–463.
- Espinosa, H.D., Zavattieri, P.D., 2003. A grain level model for the study of failure initiation and evolution in polycrystalline brittle materials. Part I: Theory and numerical implementation. *Mech. Mater.* 35, 333–364.
- Evans, A.G., Suo, Z., Wang, R.Z., Aksay, I.A., He, M.Y., Hutchinson, J.W., 2001. Model for the robust mechanical behavior of nacre. *J. Mater. Res.* 16, 2475–2484.
- Holzappel, G.A., 2000. *Nonlinear Solid Mechanics: A Continuum Approach for Engineering*. Wiley, New York.
- Jackson, A.P., Vincent, J.F.V., Turner, R.M., 1988. The mechanical design of nacre. *Proc. R. Soc. London* 234, 415–440.
- Ji, B., Gao, H., 2004. Mechanical properties of nanostructure of biological materials. *J. Mech. Phys. Solids* 52, 1963–1990.
- Katti, D.R., Katti, K.S., Sopp, J.M., Sarikaya, M., 2001. 3D finite element modeling of mechanical response in nacre-based hybrid nanocomposites. *Comput. Theor. Polym. Sci.* 11, 397–404.
- Kuhl, E., Garikipati, K., Arruda, E.M., Grosh, K., 2005. Remodeling of biological issue: mechanically induced reorientation of a transversely isotropic chain network. *J. Mech. Phys. Solids* 53, 1552–1573.
- Lubarda, V.A., 2002. *Elastoplasticity Theory*. CRC Press LLC, Boca Raton, FLA.
- Marko, J.F., Siggia, E.D., 1995. Stretching DNA. *Macromolecules* 28, 8759–8770.
- Menig, R., Meyers, M.H., Meyers, M.A., Vecchio, K.S., 2000. Quasi-static and dynamic mechanical response of *Haliotis rufescens* (abalone) shells. *Acta Mater.* 48, 2383–2398.
- Oberhauser, A.F., Marszalek, P.E., Erickson, H.P., Fernandez, M., 1998. The molecular elasticity of the extracellular matrix protein tenascin. *Nature* 393, 181–185.
- Qi, H.J., Bruet, B.F.J., Palmer, J.S., Ortiz, C., Boyce, M.C., 2005. Micromechanics and macromechanics of the tensile deformation of nacre. In: Hozappel, G.A., Ogden, R.W. (Eds.), *Mechanics of Biological Tissues, Proceedings of International Union of Theoretical and Applied Mechanics (IUTAM)*. Springer, Graz, Austria, p. 175.
- Parks, D.M., Argon, A.S., Bagepalli, B., 1984. Large elastic–plastic deformation of glassy polymers. Technical Report, MIT, Program in Polymer Science and Technology.
- Sarikaya, M., Aksay, J.A., 1992. In: Case, S. (Ed.), *Results and Problems in Cell Differentiation in Biopolymers*. Springer, Amsterdam, p. 1.
- Sarikaya, M., Gunnison, K.E., Yasrebi, M., Aksay, I.A., 1990. Mechanical property–microstructural relationships in Abalone Shell. In: Rieke, P.C., Calvert, P.D., Alper, M. (Eds.), *Materials Synthesis Utilizing Biological Processes, MRS Symp. Proc.*, Vol. 174. Material Research Society, Pittsburgh, Pennsylvania, pp. 109–116.
- Smith, B.L., Schaffer, T.E., Viani, M., Thompson, J.B., Frederick, N.A., Kindt, J., Belcher, A., Stucky, G.D., Morse, D.E., Hansma, P.K., 1999. Molecular mechanistic origin of the toughness of natural adhesives, fibres and composites. *Nature* 399, 761–763.
- Tvergaard, V., Hutchinson, J.W., 1992. The relation between crack growth resistance and fracture process parameters in elastic–plastic solids. *J. Mech. Phys. Solids* 40, 1377–1397.
- Wang, R.Z., Suo, Evans, A.G., Yao, N., Aksay, I.A., 2001. Deformation mechanisms in nacre. *J. Mater. Res.* 16, 2485–2493.
- Weber, G., Anand, L., 1990. Finite deformation constitutive equations and a time integration procedure for isotropic, hyperelastic–viscoplastic solids. *Comput. Methods Appl. Mech. Eng.* 79, 173–202.
- Wu, P.D., van der Giessen, E., 1993. On improved network models for rubber elasticity and their application to orientation hardening in glassy polymer. *J. Mech. Phys. Solids* 41, 427–456.
- Xu, X.-P., Needleman, A., 1994. Numerical simulations of fast crack growth in brittle solids. *J. Mech. Phys. Solids* 42, 1397–1434.